A Galerkin-free model reduction approach for the Navier–Stokes equations

Vilas Shinde, Elisabeth Longatte, Franck Baj, Yannick Hoarau, Marianna Braza

A Galerkin-free model reduction approach for the Navier–Stokes equations

Vilas Shinde[a,*], Elizabeth Longatte[a], Franck Baj[a],
Marianna Braza[b], Yannick Hoarau[c]

[a] *IMSIA, EDF-CNRS-CEA-ENSTA ParisTech UMR 9219, Clamart Cedex, France*
[b] *IMFT, Av. du prof. Camille Soula, 31400 Toulouse, France*
[c] *ICUBE, Strasbourg, France*

Abstract

Galerkin projection of the Navier-Stokes equations on Proper Orthogonal Decomposition (POD) basis is predominantly used for model reduction in fluid dynamics. Robustness for changing operating conditions, numerical stability for long-term transient behaviour and pressure-term consideration are still major concerns of the Galerkin Reduced-Order Models (ROMs). In this article, we present a novel interpolation based procedure to construct a solution state using reduced basis. The POD basis functions are optimal in capturing the averaged flow energy. The energy dominant POD modes and corresponding base flow are interpolated for the change in operating parameter, thereby it circumvents the Galerkin projection of Navier-Stokes equations on reduced basis as well as the time-integration of the obtained Ordinary Differential Equations (ODEs). The proposed interpolation ROM approach is thus immune from the numerical issues associated with Galerkin ROMs. The *method of snapshots* (snapshots POD) along with linear interpolation of the reduced basis are used to build the interpolation ROM. In addition, a posteriori error estimate and stability analysis of the model are formulated. A detailed case study of the flow past a cylinder at low Reynolds numbers is considered for the demonstration of proposed method. The ROM results show good agreement with the high fidelity

*Corresponding author
Email address: vilas.shinde@polytechnique.edu (Vilas Shinde)

numerical flow simulation.

Keywords:

---

1. Introduction

Computational Fluid Dynamics (CFD) simulations are indispensable element of engineering research today. Although there is considerable advancement in computing power in last couple of decades, exact flow simulations at high Reynolds numbers are unaffordable in terms of time and computing cost. The efforts become enormous for research applications (e.g. optimization) where simulations need to be performed repeatedly. Consequently, reduced-order models (ROMs) are developed extensively in recent years. They offer substantial reduction in the degrees of freedom and yet retaining the essential features of the flow by means of reduced basis. The reduced system may leads to better understanding of the underlying mechanism, thereby improvements in empirical flow (turbulence) models. Flow control, optimization and stability analysis in hydrodynamics, aero-acoustics are some of the potential applications of model reduction (see e.g. (Noack et al., 2011)).

First important step of the model reduction in fluid dynamics is to form an appropriate reduced basis from a complete set of basis functions. The choice of particular basis functions may be problem specific and the derivation can be 'a priori' or 'a posteriori'. One can refer to (Joseph, 1976), (Noack and Eckelmann, 1994) for some of the early works on 'a priori' formation of the basis functions. In the recent, (Dumon et al., 2013) used 'a priori' derivation of the basis functions, in the context of Proper General Decomposition (PGD). Besides, the spectral discretization methods are often preferred over spatial discretization methods to gain accuracy for same computing time and space requirements. In 'a posteriori' formation, the basis functions are derived using existing solution datasets with methods such as Proper Orthogonal Decomposition (POD) (e.g. method of Dynamic Mode Decomposition (DMD) in (Rowley et al., 2009) and (Schmid, 2010)). The POD (or Principle Component Analysis) is a popular choice of em-

pirical basis functions for Navier-Stokes equations. Especially, in understanding the onset of bifurcations or instabilities and spatial-temporal dynamics of the flow structures. The error in time-averaged energy remains minimal compared to every other method for the same number of modes. The convergence in extracting the space structures (topos) and associated time modes (chronos) is optimum in terms of flow energy (Aubry, 1991). An elaborated discussion and mathematical derivations on optimality of the POD method is provided in (Holmes et al., 1990).

The Galerkin ROMs are build using coordinate transformation performed by using Galerkin projection of the system of Navier-Stokes equations on the reduced basis functions. Generally, the flow velocity ($\mathbf{v}$) is decomposed in spatial ($\boldsymbol{\phi}_i$) and temporal (a_i) basis functions as shown in Equation (1) for the Galerking ROMs.

$$\mathbf{v}(\boldsymbol{x},t) \approx \mathbf{v}^{[0,1,2,\ldots n]} = \bar{\mathbf{v}}(\boldsymbol{x}) + \sum_{i=1}^{n} \boldsymbol{\phi}_i(\boldsymbol{x}) a_i(t) \tag{1}$$

Where $\bar{\mathbf{v}}(\boldsymbol{x})$ is the time-averaged base flow, n is the number of POD modes. This equation holds good under the assumption that the flow is statistically stationary in time. In incompressible flows with Dirichlet type boundary conditions, the basis functions satisfy both the boundary conditions and divergence-free constrain of the continuity equation. The Galerkin projection of momentum equations on the basis functions results in the non-linear quadratic Ordinary Differential Equations (ODEs) of the form:

$$\frac{da_i}{dt} = \mathbf{C}_i + \sum_{j}^{n} \mathbf{L}_{ij} a_j + \sum_{j,k}^{n} \mathbf{Q}_{ijk} a_j a_k \tag{2}$$

Where $\mathbf{C}, \mathbf{L}$ and $\mathbf{Q}$ are the Galerkin ROM coefficients. Equation (2) is a reduced model for the Navier-Stokes Equations (NSE) with n spatial modes. The time-integration of Equation (2) with an appropriate initial boundary condition gives the temporal basis functions, and the flow solution can be easily built by using Equation (1). The Galerkin projection ideally should preserve the stability dynamics of the NSE but generally it is achieved with extrinsic stability enablers. (Rempfer, 2000) showed how the Galerkin ROMs are inherently prone

to numerical instabilities. The energy associated with the truncated basis functions keeps piling on, that results in the divergence of ROMs. The concept of artificial viscous dissipation to stabilize the Galerkin ROM was introduced in (Aubry et al., 1988). Later, (Sirisup and Karniadakis, 2004) proposed a spectral viscosity diffusion convolution operator based on bifurcation analysis. In addition, the stability of Galerkin ROM greatly depends on parameters such as flow compressibility, pressure-term consideration, time varying boundary conditions etc. The flow compressibility effect can be considered by means of an energy based inner product to build the ROM (Rowley et al., 2004). The POD-penalty method was proposed by (Sirisup and Karniadakis, 2005) to treat the time dependence of boundary conditions on the Galerkin ROM. The Galerkin projection of the pressure-gradient term of NSE on the reduced basis functions can be neglected for internal flows. While as for open flows, the pressure term does not disappear (Noack et al., 2005) and needs to be modeled. The pressure term is accounted in the formulation of pressure extended Galerkin ROM by (Bergmann et al., 2009). In addition, (Noack et al., 2003) demonstrated that neglecting the interactions between time-averaged base flow and the fluctuating flow may lead to unstable Galerkin ROM and also introduced the concept of 'shift mode' correction technique. Further, from the flow control applications viewpoint (Morzynski et al., 2006) proposed a method in which an interpolation between stability eigenmodes and POD modes is performed to deal with changing flow conditions. A detailed discussion on numerical instabilities and perspectives of the reduced order models in fluid dynamics is provided by (Lassila et al., 2013).

An appropriate reduced basis and the Galerking projection of NSE on the reduced basis followed by the time-integration of obtained ODEs are main elements of the Galerkin ROMs. The POD basis functions are optimal choice in terms of flow energy but the Galerkin projection of NSE on the reduced basis may not produce a stable ROM as discussed above. In this article we propose a novel approach, where we completely avoid the Galerkin projection of NSE on the reduced basis and the time-integration to obtain the ROM time coefficients.

The time-averaged base flow and the POD space basis functions (topos) are interpolated for the change in operating condition. The POD temporal basis functions (chronos) are also interpolated in phase space. The periodicity (the period of limit-cycles) of the POD temporal modes is accounted for the energy conservation. The article is organised as: Section (2) is dedicated to the mathematical formulation and error analysis of the proposed ROM. In Section (3), we provide a demonstration of the method using a case study of the flow past a cylinder at low Reynolds numbers. At last, the work is summarised in Section (4).

2. Mathematical formulation

The compressible Navier-Stokes equations (including the continuity and energy equations) are considered here as the High Fidelity Model (HFM). The flow is statistically stationary in time such that Equation (1) is applicable to the solution (state) variables. The state vector $\boldsymbol{s} = \boldsymbol{s}(\boldsymbol{x}, t)$ is spanned on the space $\boldsymbol{x} \in \Omega$, Ω is the spacial flow domain. t is the time in $[0, T_\infty]$. Let H be a Hilbert space and $\boldsymbol{s} \in H$. The standard inner product, induced norm and time-average for its elements $\boldsymbol{u}, \boldsymbol{v} \in L^2(\Omega)$ are respectively,

$$(\boldsymbol{u}, \boldsymbol{v})_\Omega = \int_\Omega \boldsymbol{u} \cdot \boldsymbol{v} \, d\boldsymbol{x}, \quad ||\boldsymbol{u}||_\Omega = \sqrt{(\boldsymbol{u}, \boldsymbol{u})_\Omega} \quad \text{and} \quad \bar{\boldsymbol{u}} = \frac{1}{T_\infty} \int_{T_\infty} \boldsymbol{u} \, dt = \langle \boldsymbol{u} \rangle_{T_\infty} \quad (3)$$

2.1. Method of snapshots POD

The POD or Karhunen-Loeve expansion was first introduced in fluid dynamics by (Lumley, 1967) for the analysis of coherent structures in turbulence. Following the development of POD, (Sirovich, 1987) introduced the method of snapshots for the experimental and numerical datasets. It allows further reduction of degrees of freedom, compared to the direct method of POD.

The solution state vector $\boldsymbol{s}$ includes all variables varying in time and space. Let η be an operating parameter (e.g. Reynolds number). The state vector of

the High Fidelity Model (HFM) solution can be defined as,

$$\boldsymbol{s}(\boldsymbol{x},t;\eta) = \begin{pmatrix} \rho(\boldsymbol{x},t;\eta) \\ \mathbf{v}(\boldsymbol{x},t;\eta) \\ p(\boldsymbol{x},t;\eta) \\ \vdots \end{pmatrix} \tag{4}$$

Where ρ, $\mathbf{v}$ and p are the fluid density, velocity vector and static pressure respectively. The state vector can be separated in the time-averaged base flow and the unsteady part as shown in Equation (5).

$$\begin{aligned} \boldsymbol{s}(\boldsymbol{x},t;\eta) &= \bar{\boldsymbol{s}}(\boldsymbol{x};\eta) + \boldsymbol{s}'(\boldsymbol{x},t;\eta) & (5) \\ &= \bar{\boldsymbol{s}}(\boldsymbol{x};\eta) + \sum_{i=1}^{\infty} \boldsymbol{\phi}_i(\boldsymbol{x};\eta)\boldsymbol{a}_i(t;\eta) & (6) \end{aligned}$$

In Equation (6), the unsteady part ($\boldsymbol{s}'(\boldsymbol{x},t;\eta)$) is decomposed into the POD basis functions using Galerking expansion. The time invariant orthonormal $\boldsymbol{\phi}_i(\boldsymbol{x};\eta)$ and the space invariant orthogonal $\boldsymbol{a}_i(t;\eta)$ are the POD basis functions (modes). The state vector can be obtained in discrete (N_t) snapshots by performing a CFD simulation. The snapshots can be collected once the flow becomes statistically stationary and using (typically) a constant timestep (Δt_{sn}). Let N_t, N_{pod} be the number of snapshots and number of POD modes respectively, also $N_{pod} \leq N_{t-1}$. The state vector is approximated using discrete snapshots as,

$$\begin{aligned} \boldsymbol{s}(\boldsymbol{x},t;\eta) &\approx \boldsymbol{s}(\boldsymbol{x},t_1;\eta), ..., \boldsymbol{s}(\boldsymbol{x},t_{N_t};\eta) & (7) \\ &\approx \bar{\boldsymbol{s}}(\boldsymbol{x};\eta) + \sum_{i=1}^{N_{pod}} \boldsymbol{\phi}_i(\boldsymbol{x};\eta)\boldsymbol{a}_i(t;\eta) \qquad t_1 \leq t \leq t_{N_t} & (8) \end{aligned}$$

Where t_1 and t_{N_t} are the time coordinates of the first and last snapshots. Also, let $T_{sn} = [t_1, .., t_{N_t}]$ be the time domain of discrete snapshots collection. The time step (Δt_{sn}) of snapshots and number of snapshots (N_t) depend on the desired resolution in the temporal harmonics of the POD modes (Noack et al., 2005).

Let $\boldsymbol{R}(\eta)$ be the two point time-correlation function, given by,

$$\boldsymbol{R}(\eta) = \boldsymbol{R}(t_i,t_j,\eta) = \frac{1}{N_t}\left(\boldsymbol{s}'(\boldsymbol{x},t_i;\eta), \boldsymbol{s}'(\boldsymbol{x},t_j;\eta)\right)_{\Omega} \qquad i,j = 1,2,.....N_t \tag{9}$$

The correlation function $\boldsymbol{R}(\eta)$ is solved for the eigenvalue problem, as in Equation (11).

$$\boldsymbol{R}(\eta)\boldsymbol{\psi}_i(t;\eta) = \boldsymbol{\lambda_i}\boldsymbol{\psi}_i(t;\eta) \tag{10}$$

where $\boldsymbol{\lambda}_i$ are the eigenvalues. The orthogonal eigenfunctions $\boldsymbol{\psi}_i(t;\eta)$ are then normalized as,

$$(\boldsymbol{\psi}_i(t;\eta), \boldsymbol{\psi}_j(t;\eta))_{T_{sn}} = \boldsymbol{\delta}_{ij} \tag{11}$$

The POD modes are arranged in descending order of their energy content (the eigenvalues associated with the modes). i.e $\boldsymbol{\lambda}_1 > \boldsymbol{\lambda}_2 > \ldots\ldots\ldots\ldots > \boldsymbol{\lambda}_{N_{pod}} > 0$. The orthonormal 'topos' are obtained using Equation (12), such that $(\boldsymbol{\phi}_i(\boldsymbol{x};\eta), \boldsymbol{\phi}_i(\boldsymbol{x};\eta))_\Omega = \boldsymbol{\delta}_{ij}$.

$$\boldsymbol{\phi}_i(\boldsymbol{x};\eta) = \frac{1}{\sqrt{N_t \boldsymbol{\lambda}_i}} (\boldsymbol{s}'(\boldsymbol{x},t;\eta), \boldsymbol{\psi}_i(t;\eta))_{T_{sn}} \tag{12}$$

The corresponding POD time coefficients are given by,

$$\begin{aligned} \boldsymbol{a}_i(t;\eta) &= (\boldsymbol{\phi}_i(\boldsymbol{x};\eta), \boldsymbol{s}'(\boldsymbol{x},t;\eta))_\Omega \\ &= \sqrt{N_t \boldsymbol{\lambda}_i}\boldsymbol{\psi}_i(t;\eta) \end{aligned} \tag{13}$$

Generally, the number of reduced POD modes (N_r) is much smaller compared to the total POD modes ($N_r << N_{pod}$). The relative energy captured ($\boldsymbol{Ec}$) by the most energetic (first few) POD modes is substantial. It can be given as,

$$\%\boldsymbol{Ec} = \frac{\sum_{i=1}^{N_r} \boldsymbol{\lambda}_i}{\sum_{i=1}^{N_{pod}} \boldsymbol{\lambda}_i} \times 100 \tag{14}$$

2.2. Periodicity of POD temporal modes

The total energy [1] $\boldsymbol{E}(\eta)_{pod}$ of the unsteady part of the discrete state vector can be given by,

$$\boldsymbol{E}(\eta)_{pod} = \int_\Omega \left\langle \boldsymbol{s}'(\boldsymbol{x},t,\eta)^2 \right\rangle_{T_{sn}} d\boldsymbol{x} = \sum_{i=1}^{N_{pod}} \boldsymbol{\lambda}_i = \sum_{i=1}^{N_{pod}} \left\langle \boldsymbol{a}_i(t;\eta)^2 \right\rangle_{T_{sn}} \tag{15}$$

[1] An appropriate term for the non-velocity variables (e.g. density, pressure) be the 'variance'.

The space domain (Ω) is limited by a boundary ($\partial\Omega$). Similarly, let T_{min} be the minimum time window for which the total energy in Equation (15) remains the same, such that,

$$\boldsymbol{E}(\eta)_{pod} = \int_{\Omega} \left\langle \boldsymbol{s}'(\boldsymbol{x},t,\eta)^2 \right\rangle_{T_{min}} d\boldsymbol{x} = \sum_{i=1}^{N_{pod}} \boldsymbol{\lambda}_i = \sum_{i=1}^{N_{pod}} \left\langle \boldsymbol{a}_i(t;\eta)^2 \right\rangle_{T_{min}} \tag{16}$$

In statistically stationary flows, the POD temporal basis functions observe the stable limit cycles in phase space (see for e.g. (Sirisup and Karniadakis, 2004), (Ma and Karniadakis, 2002), (Aubry, 1991)). Let T_η be the time period of the limit-cycle of first POD time coefficient $\boldsymbol{a}_1(t;\eta)$. The higher (well resolved by snapshots) POD time modes for the state vector are periodic with the time T_η. The characteristic POD time coefficients can be defined as,

$$\tilde{\boldsymbol{a}}_i(t;\eta) = \boldsymbol{a}_i(t;\eta) \qquad for \;\; t \in [t_a, t_a + T_\eta] \tag{17}$$

Where $t_a \in [0, (T_{sn} - T_\eta)]$ is an arbitrary time. Further, the total energy in Equation (16) becomes,

$$\boldsymbol{E}(\eta)_{pod} = \sum_{i=1}^{N_{pod}} \left\langle \tilde{\boldsymbol{a}}_i(t;\eta)^2 \right\rangle_{T_\eta} = \sum_{i=1}^{N_{pod}} \left\langle \boldsymbol{a}_i(t;\eta)^2 \right\rangle_{T_{min}} = \sum_{i=1}^{N_{pod}} \boldsymbol{\lambda}_i \tag{18}$$

It also implies that the minimum time window (T_{min}) is the time period of first POD temporal mode (T_η).

Under the statistically stationary flow assumption and using periodic characteristic POD temporal modes (Equation 17), one can reconstruct the flow with reduced number (N_r) of POD basis even outside the snapshots time domain (T_{sn}) as,

$$\boldsymbol{s}(\boldsymbol{x},t;\eta) \approx \bar{\boldsymbol{s}}(\boldsymbol{x};\eta) + \sum_{i=1}^{N_r} \boldsymbol{\phi}_i(\boldsymbol{x};\eta)\tilde{\boldsymbol{a}}_i(t;\eta) \qquad t \geq 0 \tag{19}$$

2.3. Linear interpolation

The linear interpolation is used to interpolate the right hand side terms of Equation (19) for the change in operating parameter η. The interpolation of the characteristic POD temporal modes ($\tilde{\boldsymbol{a}}_i$) ensures an appropriate flow energy ($\boldsymbol{E}(\eta)$) levels in the interpolated state.

Let $\boldsymbol{s}(\boldsymbol{x}, t; \eta_j)$ with $j = 1, 2$ be the two reference states. In order to build the solution state vector at an operating parameter $\eta \in [\eta_1, \eta_2]$, the time-averaged base flow $\bar{\boldsymbol{s}}(\boldsymbol{x}; \eta)$, the POD spacial modes $(\boldsymbol{\phi}_i(\boldsymbol{x}; \eta))$ and the associated time coefficients $\tilde{\boldsymbol{a}}_i(t; \eta)$ are obtained by the interpolation of the reference states. The interpolation is formulated using a vector $\boldsymbol{\Gamma}(\boldsymbol{\beta}; \eta)$ in Equation (20). It represents either the solution state average $(\bar{\boldsymbol{s}}(\boldsymbol{x}; \eta))$ or the POD modes $(\boldsymbol{\phi}_i(\boldsymbol{x}; \eta)$ or $\tilde{\boldsymbol{a}}_i(t; \eta))$.

$$\boldsymbol{\Gamma}(\boldsymbol{\beta}; \eta) = \boldsymbol{\Gamma}(\boldsymbol{\beta}; \eta_1) + \left[\frac{(\boldsymbol{\Gamma}(\boldsymbol{\beta}; \eta_2) - \boldsymbol{\Gamma}(\boldsymbol{\beta}; \eta_1))}{(\eta_2 - \eta_1)} \right] (\eta - \eta_1) \tag{20}$$

A priori, the condition in Equation (21) is satisfied such that the interpolated quantities (RHS of Equation (19)) follow the signs of η_1 reference case.

$$(\boldsymbol{\Gamma}(\boldsymbol{\beta}; \eta_1), \boldsymbol{\Gamma}(\boldsymbol{\beta}; \eta_2))_{\boldsymbol{\beta}} \geq 0 \tag{21}$$

The time-averages of the state vectors $(\bar{\boldsymbol{s}}(\boldsymbol{x}; \eta_j)$ for $j = 1, 2)$ generally do not alter its sign for a change in the operating parameter (η_j). A symmetry in the flow geometry can lead to a phase change of π between the POD space modes $(\boldsymbol{\phi}_i(\boldsymbol{x}; \eta_j))$ for different operating conditions (η_j). The constrain in Equation (21) ensures that they do not cancel out, while performing the interpolation. In addition, the reference states η_j should be close enough, in order to perform the linear interpolation (Equation 20). The characteristic POD time coefficients $(\tilde{\boldsymbol{a}}_i(t; \eta))$ are brought in minimal phase by using Equation 21. The interpolated base solution and the POD modes follow any one of the reference states for the phase. The characteristic time period (T_η) is also linearly interpolated for a change in the operating parameter (η). The interpolation ROM, with the reduced number (N_r) of POD interpolated basis and for the change of parameter (η) in $[\eta_1, \eta_2]$, can be written as,

$$\boldsymbol{s}(\boldsymbol{x}, t; \eta) \approx \bar{\boldsymbol{s}}(\boldsymbol{x}; \eta) + \sum_{i=1}^{N_r} \boldsymbol{\phi}_i(\boldsymbol{x}; \eta) \tilde{\boldsymbol{a}}_i(t; \eta) \qquad t \geq 0 \;\; \& \;\; \eta \in [\eta_1, \eta_2] \tag{22}$$

2.4. A posteriori error estimate and stability

The High Fidelity Model (HFM) solution can be an accurate CFD solution to the full NSEs or the experimental datasets for the flow under consideration.

The HFM solution state vector can be expressed in terms of POD basis functions by Equation (6). The method of snapshots leads to an approximation (similar to Equation 8),

$$\boldsymbol{s}(\boldsymbol{x},t;\eta)_{hf} \approx \bar{\boldsymbol{s}}(\boldsymbol{x};\eta)_{pod} + \sum_{i=1}^{N_{pod}} \boldsymbol{\phi}_i(\boldsymbol{x};\eta)_{pod}\tilde{\boldsymbol{a}}_i(t;\eta)_{pod} \tag{23}$$

The subscript 'hf' stands for a high fidelity solution, while as the subscript '*pod*' stands for quantities estimated using POD. A posteriori the error in POD discretization can be given by,

$$\boldsymbol{\epsilon}_{p\boldsymbol{s}}(\boldsymbol{x},t;\eta) = \boldsymbol{s}(\boldsymbol{x},t;\eta)_{hf} - \boldsymbol{s}(\boldsymbol{x},t;\eta)_{pod} \tag{24}$$

Where the subscript '$p\boldsymbol{s}$' stands for a POD based error in the solution state vector $\boldsymbol{s}$. The POD error depends mainly on the timestep of snapshots collection (ΔT_{sn}), number of snapshots (N_t) and the time-window of snapshots collection (T_{sn}). A rigorous parametric analysis and error estimate study of the POD method was performed by Kunisch and Volkwein (2002). In order to normalise the errors, let us represent the element wise division of vectors $\boldsymbol{u}$ and $\boldsymbol{v}$ as $\boldsymbol{u} \oslash \boldsymbol{v}$, for no element of vector $\boldsymbol{v}$ is zero ($v_i \neq 0$). Further, the total variance can be defined for the high fidelity state vector $\boldsymbol{s}(\boldsymbol{x},t;\eta)$ as,

$$\boldsymbol{\sigma}^2(\eta) = \int_{\Omega} \left\langle \boldsymbol{s}'(\boldsymbol{x},t;\eta)^2_{hf} \right\rangle_{T_\infty} d\boldsymbol{x} \tag{25}$$

A posteriori, normalized error in POD discretization can be given by,

$$\epsilon_p(t;\eta) = \left|\left| \int_{\Omega} \boldsymbol{\epsilon}_{p\boldsymbol{s}}(\boldsymbol{x},t;\eta)^2 d\boldsymbol{x} \oslash \boldsymbol{\sigma}^2(\eta) \right|\right|_{r(\boldsymbol{s})} \tag{26}$$

Where $r(\boldsymbol{s})$ stands for number of state variables. In addition, the error introduced by truncation of the higher ($> N_r$) POD modes can be obtained as,

$$\boldsymbol{\epsilon}_{t\boldsymbol{s}}(\boldsymbol{x},t;\eta) = \sum_{i=N_r+1}^{N_{pod}} \boldsymbol{\phi}_i(\boldsymbol{x};\eta)_{pod}\, \tilde{\boldsymbol{a}}_i(t;\eta)_{pod} \tag{27}$$

The normalized truncation error becomes,

$$\epsilon_t(t;\eta) = \left|\left| \int_{\Omega} \boldsymbol{\epsilon}_{t\boldsymbol{s}}(\boldsymbol{x},t;\eta)^2 d\boldsymbol{x} \oslash \boldsymbol{\sigma}^2(\eta) \right|\right|_{r(\boldsymbol{s})} \tag{28}$$

2.4.1. Interpolation error

The interpolation error associated with each term can be defined as,

$$\begin{aligned}
\boldsymbol{\epsilon}_{\bar{\boldsymbol{s}}}(\boldsymbol{x};\eta) &= \bar{\boldsymbol{s}}(\boldsymbol{x};\eta)_{pod} - \bar{\boldsymbol{s}}(\boldsymbol{x};\eta) \\
\boldsymbol{\epsilon}_{\boldsymbol{\phi}_i}(\boldsymbol{x};\eta) &= \boldsymbol{\phi}_i(\boldsymbol{x};\eta)_{pod} - \boldsymbol{\phi}_i(\boldsymbol{x};\eta) \\
\boldsymbol{\epsilon}_{\tilde{\boldsymbol{a}}_i}(t;\eta) &= \tilde{\boldsymbol{a}}_i(t;\eta)_{pod} - \tilde{\boldsymbol{a}}_i(t;\eta)
\end{aligned} \tag{29}$$

A combined interpolation error at a time instance can be formulated for the reduced POD basis (N_r) as,

$$\begin{aligned}
\boldsymbol{\epsilon}_{i\boldsymbol{s}}(\boldsymbol{x},t;\eta) = \boldsymbol{\epsilon}_{\bar{\boldsymbol{s}}}(\boldsymbol{x};\eta) + \\
\sum_{i=1}^{N_r} \boldsymbol{\phi}_i(\boldsymbol{x};\eta)\boldsymbol{\epsilon}_{\tilde{\boldsymbol{a}}_i}(t;\eta) + \boldsymbol{\epsilon}_{\boldsymbol{\phi}_i}(\boldsymbol{x};\eta)\tilde{\boldsymbol{a}}_i(t;\eta) + \boldsymbol{\epsilon}_{\boldsymbol{\phi}_i}(\boldsymbol{x};\eta)\boldsymbol{\epsilon}_{\tilde{\boldsymbol{a}}_i}(t;\eta)
\end{aligned} \tag{30}$$

A priori, the maximum error bound in the linear interpolation can be given by Equation (31), for each interpolation error term from Equation (30). The second derivatives ($\boldsymbol{\alpha}_*$) must exist.

$$\begin{aligned}
|\boldsymbol{\epsilon}_{\bar{\boldsymbol{s}}}(\boldsymbol{x};\eta)| &\leq \frac{1}{8}(\Delta\eta)^2 \sup_{\eta\in[\eta_1,\eta_2]} |\boldsymbol{\alpha}_{\bar{\boldsymbol{s}}}(\boldsymbol{x};\eta)| \quad \text{where } \boldsymbol{\alpha}_{\bar{\boldsymbol{s}}}(\boldsymbol{x};\eta) = \frac{\partial^2}{\partial\eta^2}(\bar{\boldsymbol{s}}(\boldsymbol{x};\eta)_{pod}) \\
|\boldsymbol{\epsilon}_{\boldsymbol{\phi}_i}(\boldsymbol{x};\eta)| &\leq \frac{1}{8}(\Delta\eta)^2 \sup_{\eta\in[\eta_1,\eta_2]} |\boldsymbol{\alpha}_{\boldsymbol{\phi}_i}(\boldsymbol{x};\eta)| \quad \text{where } \boldsymbol{\alpha}_{\boldsymbol{\phi}_i}(\boldsymbol{x};\eta) = \frac{\partial^2}{\partial\eta^2}(\boldsymbol{\phi}_i(\boldsymbol{x};\eta)_{pod}) \\
|\boldsymbol{\epsilon}_{\tilde{\boldsymbol{a}}_i}(t;\eta)| &\leq \frac{1}{8}(\Delta\eta)^2 \sup_{\eta\in[\eta_1,\eta_2]} |\boldsymbol{\alpha}_{\tilde{\boldsymbol{a}}_i}(t;\eta)| \quad \text{where } \boldsymbol{\alpha}_{\tilde{\boldsymbol{a}}_i}(t;\eta) = \frac{\partial^2}{\partial\eta^2}(\tilde{\boldsymbol{a}}_i(t;\eta)_{pod})
\end{aligned} \tag{31}$$

The error is $\mathcal{O}(\Delta\eta^2)$. Here $\Delta\eta = (\eta_2 - \eta_1)$. The value of $\Delta\eta$ can be chosen based on the total interpolation error bound $|\boldsymbol{\epsilon}_{i\boldsymbol{s}}(\boldsymbol{x},t;\eta)|$. The total interpolation error in the solution state vector $\boldsymbol{s}(\boldsymbol{x},t;\eta)$ is in bounds as,

$$\begin{aligned}
|\boldsymbol{\epsilon}_{i\boldsymbol{s}}(\boldsymbol{x},t;\eta)| \leq \frac{1}{8}(\Delta\eta)^2 \sup_{\eta\in[\eta_1,\eta_2]} \Bigg| \boldsymbol{\alpha}_{\bar{\boldsymbol{s}}}(\boldsymbol{x};\eta) + \sum_{i=1}^{N_r} \boldsymbol{\phi}_i(\boldsymbol{x};\eta)\boldsymbol{\alpha}_{\tilde{\boldsymbol{\alpha}}_i}(t;\eta) + \\
\boldsymbol{\alpha}_{\boldsymbol{\phi}_i}(\boldsymbol{x};\eta)\tilde{\boldsymbol{a}}_i(t;\eta) + \frac{1}{8}(\Delta\eta)^2\boldsymbol{\alpha}_{\boldsymbol{\phi}_i}(\boldsymbol{x};\eta)\boldsymbol{\alpha}_{\tilde{\boldsymbol{\alpha}}_i}(t;\eta) \Bigg|
\end{aligned} \tag{32}$$

On the other hand, the interpolation error can be a posteriori given by,

$$\boldsymbol{\epsilon}_{i\boldsymbol{s}}(\boldsymbol{x},t;\eta) = \left(\bar{\boldsymbol{s}}(\boldsymbol{x};\eta)_{pod} + \sum_{i=1}^{N_r} \boldsymbol{\phi}_i(\boldsymbol{x};\eta)_{pod}\tilde{\boldsymbol{a}}_i(t;\eta)_{pod}\right) - \left(\bar{\boldsymbol{s}}(\boldsymbol{x};\eta) + \sum_{i=1}^{N_r} \boldsymbol{\phi}_i(\boldsymbol{x};\eta)\tilde{\boldsymbol{a}}_i(t;\eta)\right) \quad (33)$$

The normalized interpolation error will be,

$$\epsilon_i(t;\eta) = \left|\left|\int_\Omega \boldsymbol{\epsilon}_{i\boldsymbol{s}}(\boldsymbol{x},t;\eta)^2 d\boldsymbol{x} \oslash \boldsymbol{\sigma}^2(\eta)\right|\right|_{r(\boldsymbol{s})} \quad (34)$$

Generally, the error in Galerkin ROMs is quantified based on quadratic flow energy terms. The POD basis functions (topos and chronos) are the optimal basis for ROM in fluid dynamics, hence provide an upper bound for the error in Gelerkin ROM ((Balajewicz and Dowell, 2012), (Demmel, 1997)). The normalized error in ROM based on the kinetic energy can be expressed as,

$$\begin{aligned} \epsilon_e(t;\eta) &= \left|\left|(\boldsymbol{E}(t;\eta)_{pod} - \boldsymbol{E}(t;\eta)) \oslash \boldsymbol{\sigma}^2(\eta)\right|\right|_{r(\boldsymbol{s})} \\ &= \left|\left|\left(\sum_{i=1}^{N_{pod}} \tilde{\boldsymbol{a}}_i(t;\eta)^2_{pod} - \sum_{i=1}^{N_r} \tilde{\boldsymbol{a}}_i(t;\eta)^2\right) \oslash \boldsymbol{\sigma}^2(\eta)\right|\right|_{r(\boldsymbol{s})} \end{aligned} \quad (35)$$

The energy based error ($\epsilon_e(t;\eta)$) does not account for the error in interpolation of the time-averaged base flow ($\bar{\boldsymbol{s}}(\boldsymbol{x};\eta)$) as well as the POD space modes ($\boldsymbol{\phi}_i(\boldsymbol{x};\eta)$). Therefore the total error relevant to the interpolation ROM can be defined as,

$$\epsilon_{it}(t;\eta) = \epsilon_i(t;\eta) + \epsilon_t(t;\eta) \quad (36)$$

2.4.2. Stability of the interpolation ROM

Almost all the Galerkin ROMs are unstable and need stabilization techniques such as, artificial viscosity terms, increasing order of the ROMs. This way either the high fidelity Navier-Stokes equation are altered or the computational efforts are increased (Balajewicz and Dowell, 2012). On the contrary, the interpolation based approach of ROM uses flow stationarity for the energy balance instead of considering the energy of truncated POD modes in terms of empirical turbulence

models. The time average of the total error $\epsilon_{it}(t;\eta)$ in the interpolation ROM (Equation (36)) can be given by,

$$\epsilon(\eta) = \langle \epsilon_{it}(t;\eta) \rangle_{T_\infty} = \langle \epsilon_{it}(t;\eta) \rangle_{T_\eta} \tag{37}$$

it implies,

$$\frac{\partial \epsilon(\eta)}{\partial T_\eta} = 0 \tag{38}$$

The errors ($\boldsymbol{\epsilon_{ps}}(\boldsymbol{x},t;\eta)$, $\boldsymbol{\epsilon_{ts}}(\boldsymbol{x},t;\eta)$ and $\boldsymbol{\epsilon_{is}}(\boldsymbol{x},t;\eta)$) in the interpolation ROM are in bounds under the stationary flow assumption for all time. The total normalized error $\epsilon(\eta)$ remains a function of the parameters ΔT_{sn}, N_t, N_{pod}, N_r, $\Delta\eta$ and the second derivatives $\boldsymbol{\alpha_{\bar{s}}}$, $\boldsymbol{\alpha_{\phi_i}}$ and $\boldsymbol{\alpha_{\bar{a}_i}}$.

3. Flow past a cylinder at low Reynolds number - a case study

A compressible Navier-Stokes flow solver (Navier-Stokes Multi Block - NSMB) is used with a preconditioning for the incompressible flow at low Mach number. The NSMB solver is developed in collaboration between several European organizations which mainly includes Airbus, KTH, EPFL, IMFT, ICUBE, CERFACS, University of Karlsruhe and ETH-Ecole Polytechnique de Zurich. The code has been developed since early 90's. It is coordinated by CFS Engineering in Lausanne, Switzerland. NSMB is a structured code including a variety of high-order numerical schemes and turbulence modeling such as LES, URANS, RANS-LES hybrid turbulence modeling, especially DDES (Delayed Detached Eddy Simulations).

The flow past a cylinder at low Reynolds number ($Re = 125 \sim 150$) in 2-dimension (2D) is considered for the demonstration of the proposed Reduced-Order Model (ROM). Figure (1) shows the flow domain and the instantaneous flow fields (u, v and p) at Reynolds number $Re = 125$ ($Re = \rho u_\infty D/\mu$). The cylinder of diameter $D = 1$ is at the center of the computational domain. The inflow streamwise (along $+x$ axis) velocity (u_∞) as well as the temperature (θ_∞) far upstream are set to 1. The density of the fluid (calorically perfect gas) is $\rho = 1$. The Mach number upstream is $M_\infty = 0.18$, while as the specific

heat ratio of 1.4 (for air) is taken. The gas constant R and the inflow pressure p_∞ are 22.05. The dynamic viscosity (μ) is constant, it is estimated using the Reynolds number (Re_∞) as, $\mu = (\rho \mathbf{v}_\infty D)/(Re_\infty)$. The inflow transverse velocity is $v_\infty = 0$. The internal energy (e) and the enthalpy (h) are given by $C_v\theta$ and $C_p\theta$ respectively, where C_v, C_p are the specific heats at constant volume and constant pressure respectively. The total energy (E) and the internal energy (e) are related by

$$e = E - \frac{1}{2}\left(u^2 + v^2\right))$$

3.1. Governing flow equations and numerical methods

The compressible unsteady Navier-Stokes equations in 2D can be written as,

$$\frac{\partial}{\partial t}(\boldsymbol{w}) + \frac{\partial}{\partial x}(\boldsymbol{f} - \boldsymbol{f}_\nu) + \frac{\partial}{\partial y}(\boldsymbol{g} - \boldsymbol{g}_\nu) = 0 \tag{39}$$

Where,

$$\begin{aligned}
\boldsymbol{w} &= \begin{pmatrix} \rho \\ \rho u \\ \rho v \\ \rho E \end{pmatrix}, \boldsymbol{f} = \begin{pmatrix} \rho u \\ \rho u^2 + p \\ \rho uv \\ u(\rho E + p) \end{pmatrix}, \boldsymbol{g} = \begin{pmatrix} \rho v \\ \rho vu \\ \rho v^2 + p \\ v(\rho E + p) \end{pmatrix} \\
\boldsymbol{f}_\nu &= \begin{pmatrix} 0 \\ \tau_{xx} \\ \tau_{xy} \\ [\boldsymbol{\tau}, \mathbf{v}]_x - q_x \end{pmatrix}, \boldsymbol{g}_\nu = \begin{pmatrix} 0 \\ \tau_{yx} \\ \tau_{yy} \\ [\boldsymbol{\tau}, \mathbf{v}]_y - q_y \end{pmatrix}
\end{aligned}$$

Here $\boldsymbol{w}$ is the state vector. $\boldsymbol{f}$, $\boldsymbol{g}$ are the convective fluxes, while as $\boldsymbol{f}_\nu$, $\boldsymbol{g}_\nu$ are the viscous fluxes. The components of shear stress tensor $\boldsymbol{\tau}$ in the viscous fluxes are given by Equation (40).

$$\begin{aligned}
\tau_{xx} &= \frac{2}{3}\mu\left(2\frac{\partial u}{\partial x} - \frac{\partial v}{\partial y}\right), \tau_{yy} = \frac{2}{3}\mu\left(-\frac{\partial u}{\partial x} + 2\frac{\partial v}{\partial y}\right) \\
\tau_{xy} &= \tau_{yx} = \mu\left(\frac{\partial u}{\partial y} + \frac{\partial v}{\partial x}\right)
\end{aligned} \tag{40}$$

The heat flux is calculated using Fourier's law as,

$$q_x = -k\frac{\partial \theta}{\partial x}, q_y = -k\frac{\partial \theta}{\partial y} \qquad \text{with } \; k = \mu C_p/Pr \tag{41}$$

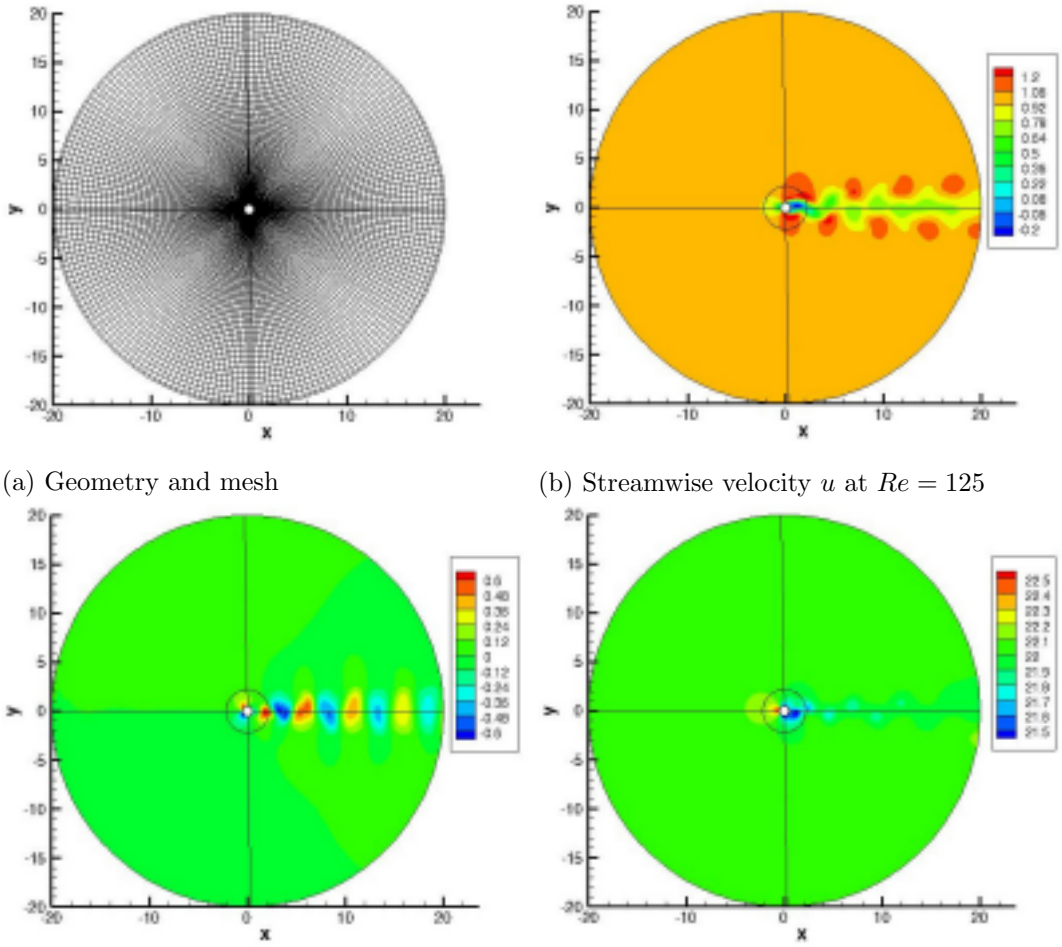

(a) Geometry and mesh

(b) Streamwise velocity u at $Re = 125$

(c) Transverse velocity v at $Re = 125$

(d) Pressure p at $Re = 125$

Figure 1: Computational domain and instantaneous flow fields at $Re = 125$

Where k is the thermal conductivity. The Prandtl number (Pr) is taken 0.72 (for air).

The second order fully implicit LU-SGS (Lower-Upper Symmetric Gauss-Seidel) backward A-stable scheme with a dual-time stepping is used for the time marching. The space discretization is done using forth order central finite volume scheme in a skew-symmetric form. The preconditioning method proposed in (Turkel et al., 1996) to impose the incompressibility is used, for the

flows at low speed (mach number).

3.2. Results and discussion

The state vector $\boldsymbol{s}$ in the case study (2-D, incompressible flow) can be considered as,

$$\boldsymbol{s}(\boldsymbol{x}, t; \eta) = \begin{pmatrix} u(\boldsymbol{x}, t; \eta) \\ v(\boldsymbol{x}, t; \eta) \\ p(\boldsymbol{x}, t; \eta) \end{pmatrix} \tag{42}$$

Where $\boldsymbol{x}$ is the space domain with x and y dimensions. t represents the time. The operating parameter η is the Reynolds number Re. The two reference cases are considered at Reynolds numbers $\eta_1 = Re_1 = 125$ and $\eta_2 = Re_2 = 150$. The number of snapshots taken for each reference case is $N_t = 900$, this constitutes ≈ 14 vortex shedding periods. The time step for snapshots collection is $\Delta t_{sn} = 0.05$. The correlation matrix was built for each reference case and solved for the eigenvalue problem as detailed in Section (2.1). The off-reference case is considered at $\eta = Re = 140$. The linear interpolation of the state vector time-averages and POD modes (both topos and chronos) using the reference states is performed as per Section (2.3). The results are build using first 10 POD modes ($N_r = 10$) out of 500 POD modes ($N_{pod} = 500$) and compared with the Navier-Stokes High Fidelity Model (HFM) simulation results at the same Reynolds number.

The results of POD analysis at $Re = 140$ are shown is Figure (2), in terms of the eigenvalues and the time evolution of the discretization error involved in the method of snapshots POD. Figure 2(a) shows the % energy associated with each POD mode of the state variables. It also indicates that the $\approx 99.99\%$ of total energy is contained in first 10 modes of each state variables. Therefore the number of reduced basis $N_r = 10$ is chosen for the interpolation (ROM). The discretization error in the method of snapshots POD ($\epsilon_p(t; \eta)$), as defined in Equation (26) is plotted in Figure 2(b). The root-mean-srquared (rms) of the error is $\approx 0.25\%$ of the variance of the state variable.

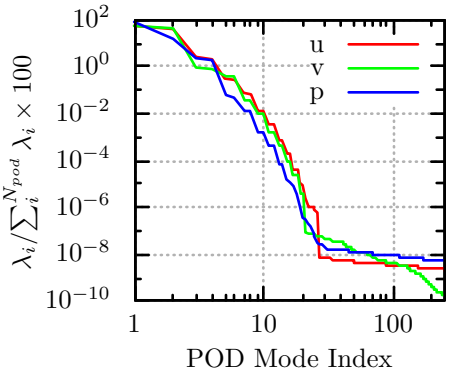

(a) % energy associated with each POD mode of u, v and p.

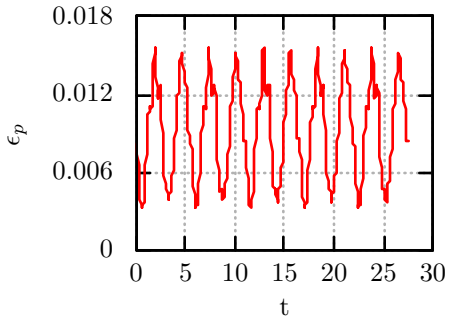

(b) The POD discretization error ($\epsilon_p(t; Re)$, as defined in Equation (26))

Figure 2: POD analysis of the flow at $Re = 140$ (η)

3.2.1. Interpolation of the POD reduced basis

In this case study, the POD space modes ($\boldsymbol{\phi}_i(\boldsymbol{x}; \eta)$) are either symmetric or antisymmetric about the x axis. The preconditioning in Equation (21) is needed for the antisymmetric modes, only when they observe a flip of sign in changing operating condition (η). Figure (3) shows the linear interpolation performed for the fifth space mode of the streamwise velocity (ϕ_5^u). Figures 3(a) and 3(b) are the fifth POD space modes of the reference cases at $Re_1 = 125$ and $Re_2 = 150$ respectively. The result of interpolation at $Re = 140$ for $\phi_5^u(\boldsymbol{x}; Re)$ is shown in Figure 3(d). Figure 3(c) shows the actual POD mode (ϕ_5^u) at $Re = 140$, computed using the method of snapshots POD for comparison with the interpolated mode.

Similarly, the remaining topos from the reduced basis were interpolated at Reynolds number $Re = 140$. Figure (4) shows comparison of the first four interpolated (ROM) modes (Figures 4(b), 4(d), 4(f), 4(h)) versus the snapshots POD modes (Figures 4(a), 4(c), 4(e), 4(g) respectively). One can notice that the POD modes act in pairs. The first pair of POD modes of streamwise velocity u (mode number 1 & 2) is antisymmetric, while the second one is symmetric about the x axis. In general here, the odd pairs of POD modes of u are antisymmetric

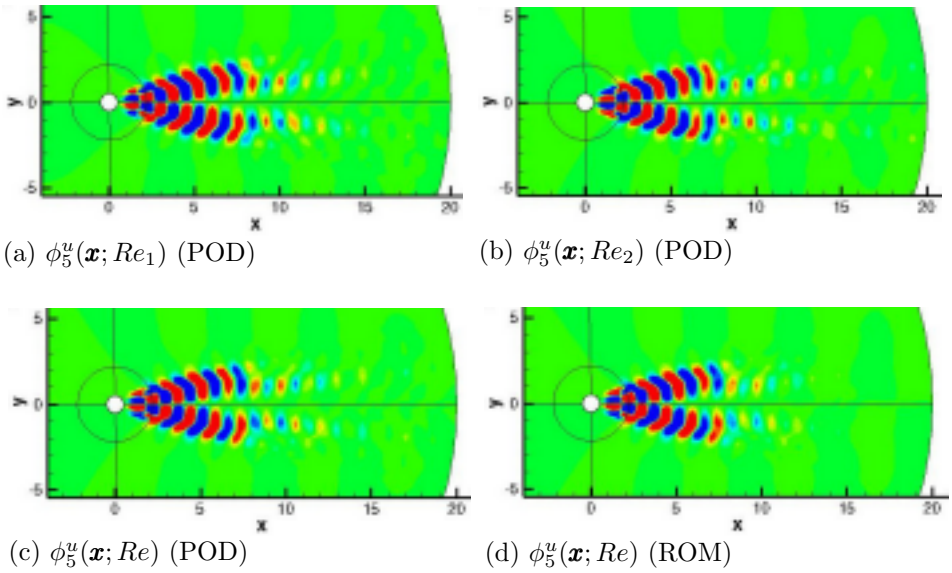

(a) $\phi_5^u(\boldsymbol{x}; Re_1)$ (POD) (b) $\phi_5^u(\boldsymbol{x}; Re_2)$ (POD)

(c) $\phi_5^u(\boldsymbol{x}; Re)$ (POD) (d) $\phi_5^u(\boldsymbol{x}; Re)$ (ROM)

Figure 3: Interpolation of $\phi_5^u(\boldsymbol{x}, \cdot)$

and the even pairs are symmetric. The antisymmetry of the modes about x axis is dealt by the constrain in Equation (21) before interpolating the modes. The POD is a biorthogonal decomposition of the flow in space and time, there is one-to-one correspondence between topos and chronos (Aubry, 1991). The change in symmetry of a topo reflects in the corresponding chrono. Although this change of sign (of $\boldsymbol{\phi}_i$ and $\tilde{\boldsymbol{a}}_i$ for the same operating condition) does not alter the value of flow reconstruction by Equation (22). The phase information is anyway lost because of the second order statistics used in the POD basis functions (Schmid, 2010). In addition to the phase information, the change of operating condition (Re) leads to the change in orientation of the POD basis functions. The interpolation procedure ensures an appropriate orientation of the POD reduced basis for an intermediate operating conditions between the reference states.

In Galerkin ROMs the time coefficients often need corrections in their amplitudes. The common source of error is due to the truncation of higher POD modes and the formulation of the ROM without pressure-term representation.

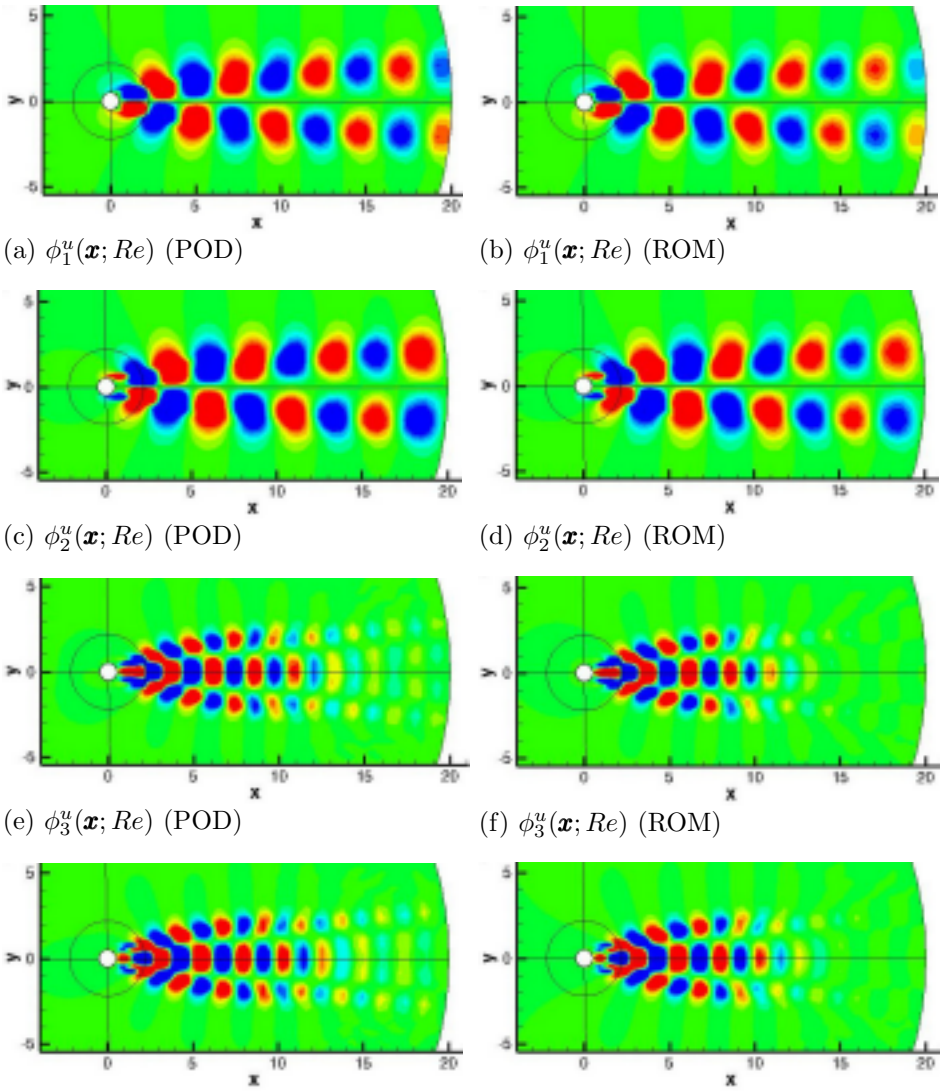

(a) $\phi_1^u(\boldsymbol{x}; Re)$ (POD) (b) $\phi_1^u(\boldsymbol{x}; Re)$ (ROM)

(c) $\phi_2^u(\boldsymbol{x}; Re)$ (POD) (d) $\phi_2^u(\boldsymbol{x}; Re)$ (ROM)

(e) $\phi_3^u(\boldsymbol{x}; Re)$ (POD) (f) $\phi_3^u(\boldsymbol{x}; Re)$ (ROM)

(g) $\phi_4^u(\boldsymbol{x}; Re)$ (POD) (h) $\phi_4^u(\boldsymbol{x}; Re)$ (ROM)

Figure 4: Comparison of $\phi_1^u(\boldsymbol{x}, Re)$ to $\phi_4^u(\boldsymbol{x}, Re)$ modes obtained by the snapshots POD against the modes obtained using linear interpolation (ROM) at $Re = 140$

For instance, the Galerkin ROMs without pressure-term consideration leads to higher amplitudes of the POD time coefficients (Noack et al. 2005). The characteristic POD time coefficients ($\tilde{\boldsymbol{a}}_i(t; Re)$) are immune from the truncation and pressure-term errors, since they are extracted from the time coefficients of the

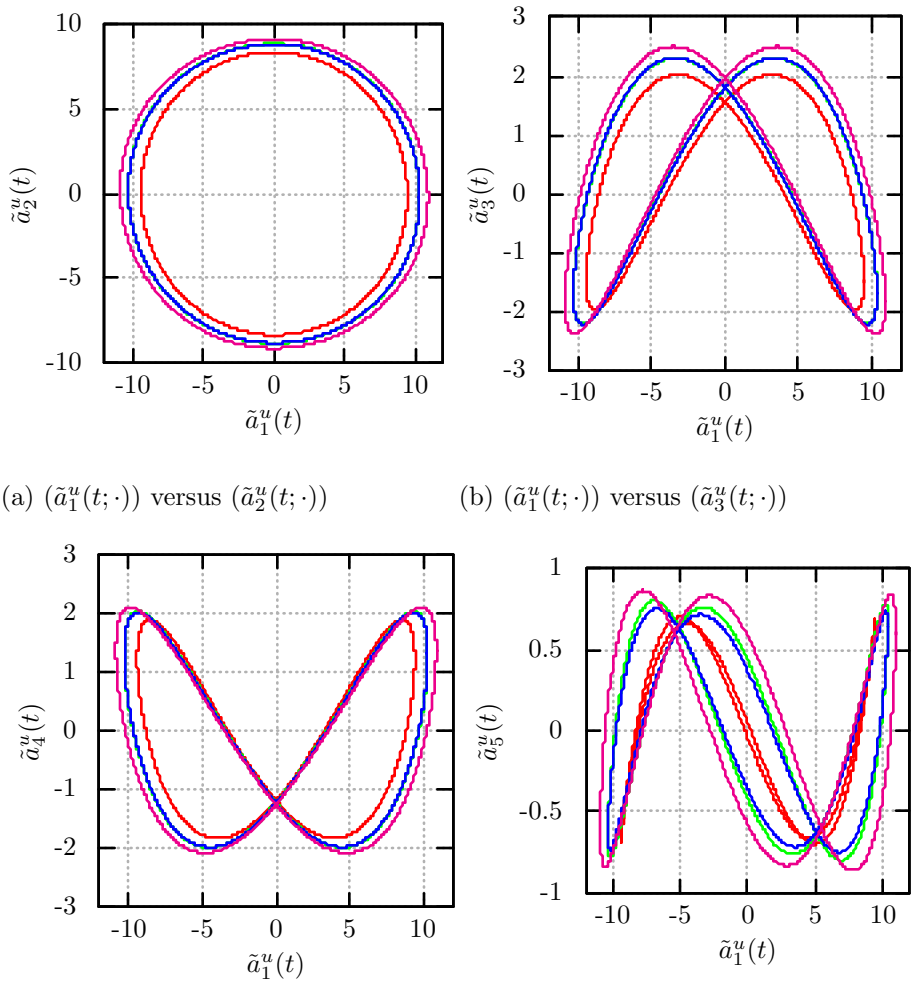

(a) $(\tilde{a}_1^u(t;\cdot))$ versus $(\tilde{a}_2^u(t;\cdot))$

(b) $(\tilde{a}_1^u(t;\cdot))$ versus $(\tilde{a}_3^u(t;\cdot))$

(c) $(\tilde{a}_1^u(t;\cdot))$ versus $(\tilde{a}_4^u(t;\cdot))$

(d)$(\tilde{a}_1^u(t;\cdot))$ versus $(\tilde{a}_5^u(t;\cdot))$

Figure 5: Comparison of the time coefficients $\tilde{a}_i^u(T.;\cdot)$ of the first five chronos. The blue curve in each plot is an interpolated mode (ROM) at $Re = 140$ against the snapshot POD mode at $Re = 140$ in green. The other color correspondence with Reynolds numbers is: Red $\rightarrow Re_1 = 125$ and Pink $\rightarrow Re_2 = 150$

POD $(\boldsymbol{a}_i(t;Re))$ itself as per Equation (17) for the reference cases (η_1 and η_2). The characteristic time coefficients, similar to the fellow spacial modes act in pairs. The interpolation results for the characteristic time coefficients (chronos)

are shown in Figure (5). It shows the comparison of interpolation results in phase space for the first five characteristic time coefficients. The curves in each plot (Figures 5(a), 5(b), 5(c) and 5(d)) expand in size, with the increase of Reynolds number. The limit-cycles represented in red color are for the reference state $Re_1 = 125$, while the ones in pink color are for the reference state $Re_2 = 150$. The limit-cycles at $Re = 140$, in blue color are interpolated using the reference states Re_1 and Re_2. It can be compared with the characteristic POD time modes obtained using snapshots POD at $Re = 140$ in green color.

In addition, the characteristic times (T_η) of the reference states $Re_1 = 125$ and $Re_2 = 150$ are $T_{Re_1} = 5.647$ and $T_{Re_2} = 5.400$ respectively. The linearly interpolated characteristic time at $Re = 140$ is $T_{Re} = 5.499$ against the value 5.489 obtained in POD analysis.

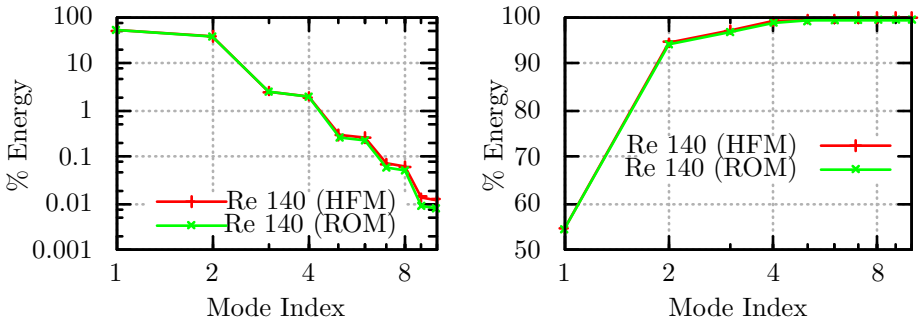

(a) Energy (eigen values) comparison (b) Cumulative energy comparison

Figure 6: Energy comparison of the interpolated (ROM) modes with the snapshots POD modes

The eigenvalues of the interpolation ROM solution at $Re = 140$ were estimated using relation,

$$\boldsymbol{\lambda}_i = \left\langle \tilde{\boldsymbol{a}}_i(t; Re)^2 \right\rangle_{T_{Re}} \tag{43}$$

Figure 6(a) shows the energy (in %) associated with the reduced interpolated (ROM) modes at $Re = 140$, it is compared with the energy (in %) of the corresponding snapshots POD modes (cumulative plot in Figure 6(b)). The time-averaged flow energy estimation using the interpolated POD time modes

(Equation 43) evinces the orthogonality of the interpolated modes (Balajewicz and Dowell, 2012). An additional orthogonality check is performed a posteriori on the interpolated reduced basis. The angle ($\theta_{\boldsymbol{\gamma},\boldsymbol{\beta}}$) between interpolated modes ($\boldsymbol{\gamma}$, $\boldsymbol{\beta} \in L^2(\Omega)$) is calculated by means of their inner product as,

$$\theta_{\boldsymbol{\gamma},\boldsymbol{\beta}} = \arccos\left(\frac{(\boldsymbol{\gamma},\boldsymbol{\beta})_\Omega}{||\boldsymbol{\gamma}||_\Omega ||\boldsymbol{\beta}||_\Omega}\right) \tag{44}$$

The angles (in degree) between the interpolated reduced basis of streamwise velocity (u) are tabulated in Table (1). It clearly demonstrates that the interpolation of the POD modes retains the orthogonality of both the topos ($\boldsymbol{\phi}_i$) and chronos ($\tilde{\boldsymbol{a}}_i$).

	ϕ_1^u	ϕ_2^u	ϕ_3^u	ϕ_4^u	ϕ_5^u	ϕ_6^u	ϕ_7^u	ϕ_8^u	ϕ_9^u	ϕ_{10}^u
ϕ_1^u	00.0	89.9	89.9	90.4	90.1	90.0	90.0	90.0	90.0	90.1
ϕ_2^u	89.9	00.0	90.4	90.1	89.8	90.0	90.0	90.0	90.0	90.0
ϕ_3^u	89.9	90.4	00.0	90.4	89.8	90.5	90.1	89.9	90.0	90.0
ϕ_4^u	90.4	90.2	90.4	00.0	90.5	90.3	90.1	89.8	90.0	90.0
ϕ_5^u	90.1	89.8	89.8	90.5	00.0	89.8	90.3	89.7	90.5	89.9
	$\tilde{a}_1^u$	$\tilde{a}_2^u$	$\tilde{a}_3^u$	$\tilde{a}_4^u$	$\tilde{a}_5^u$	$\tilde{a}_6^u$	$\tilde{a}_7^u$	$\tilde{a}_8^u$	$\tilde{a}_9^u$	$\tilde{a}_{10}^u$
$\tilde{a}_1^u$	00.0	90.1	89.0	89.3	90.2	89.7	89.5	90.4	90.4	90.3
$\tilde{a}_2^u$	90.1	00.0	88.7	90.3	91.6	91.3	90.1	90.5	90.3	88.3
$\tilde{a}_3^u$	89.0	88.7	00.0	90.5	91.7	88.3	90.2	88.0	90.3	89.7
$\tilde{a}_4^u$	89.3	90.3	90.5	00.0	88.1	88.0	90.8	89.6	89.6	91.0
$\tilde{a}_5^u$	90.2	91.6	91.7	88.1	00.0	89.9	87.8	94.0	91.4	90.3

Table 1: Orthogonality (angle between the modes in degree) of the interpolated reduced basis

The errors quantification, as formulated in Section (2.4) is plotted in Figure (7). The truncation error ($\epsilon_t(t; Re)$) is nothing but the contribution of higher order POD basis functions ($N_{pod} - N_r$) to the fluctuations in state variables. The maximum truncation error is $\approx 0.25\%$ of the variance (σ^2) for each state variable (Figure 7(a)). The interpolation error ($\epsilon_i(t; Re)$) is relatively high, the maximum of it is about 2% of the variance, for $\Delta\eta = \Delta Re = 25$. The total error

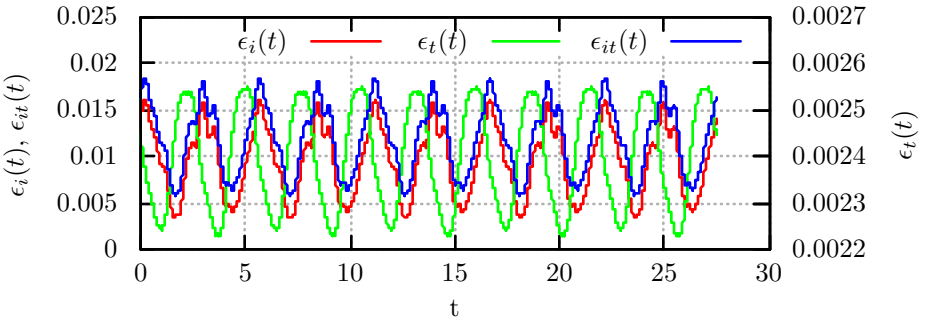

(a) ϵ_i, ϵ_t & ϵ_{it} - a time evolution

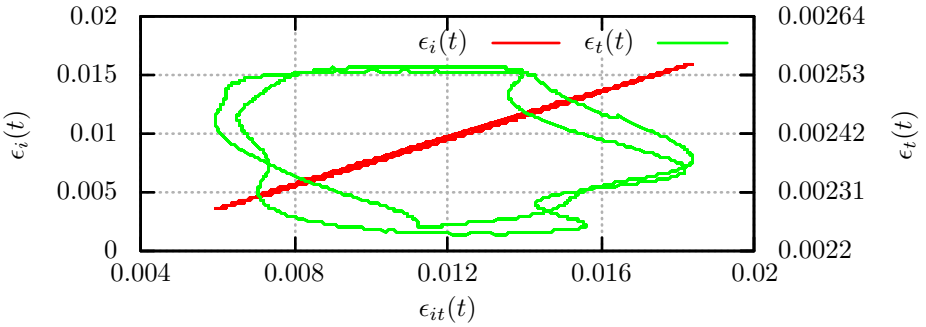

(b) ϵ_i, ϵ_t & ϵ_{it} - in phase space

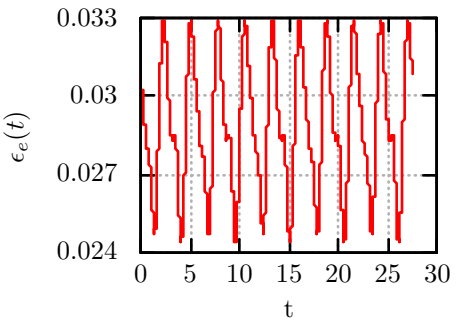

(c) $\epsilon_e(t; Re)$

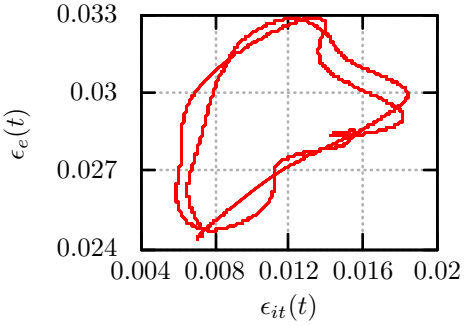

(d) ϵ_e in phase space with ϵ_{it}

Figure 7: Time evolution and phase diagrams of the Errors

relevant to the interpolation ROM ($\epsilon_{it}(t; Re)$) is also ~ 10 times the truncation error. Figure 7(b) shows the errors (ϵ_i, ϵ_t & ϵ_{it}) in phase space. The limit cycles illustrate the boundedness of errors amplitude with the time evolution. On the other hand, maximum of the energy based error $\epsilon_e(t; Re)$ (as defined

in Equation (35)) is ≈ 22% of the variance (Figure 7(c)). Further, the phase diagrams in Figure 7(b) and Figure 7 (d) show that the errors follow the stable limit cycles, demonstrating the stability of interpolation ROM method.

3.2.2. High fidelity solution comparisons

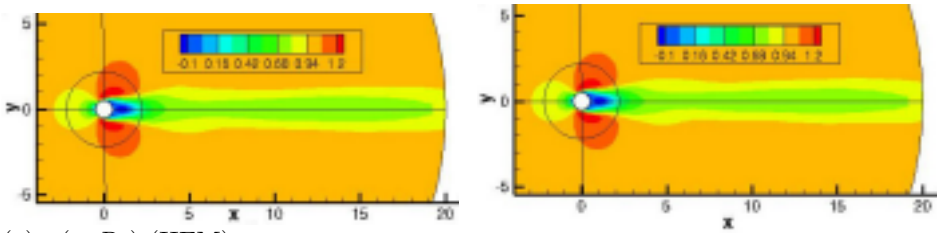

(a) $\bar{u}(\boldsymbol{x}; Re)$ (HFM) (b) $\bar{u}(\boldsymbol{x}; Re)$ (ROM)

Figure 8: Time-averaged base flow comparison at $Re = 140$ ($\bar{u}(\boldsymbol{x}, Re)$)

Figure 8(a) shows the average of streamwise velocity $\bar{u}(\boldsymbol{x}; Re)$ obtained using the high fidelity computational fluid dynamics (CFD) simulation at Reynolds number $Re = 140$. The interpolated time-average of the streamwise velocity at same Reynolds number ($Re = 140$) using the reference states at $Re = 125$ and $Re = 150$ is shown in Figure 8(b). Generally, the time-averaged base flow shows little variation over the long range of Reynolds numbers. In addition, the dimensionless quantities of practical importance such as Drag, Lift coefficients vary with the logarithmic change in Reynolds number. Therefore the second derivatives $\boldsymbol{\alpha}_*$ in Equation (32), contributing to the error bounds for the interpolation error can expected to be small, providing the possibility to have larger $\Delta\eta$. Figure 9(a) shows the phase plot of the Drag versus Lift coefficients estimated using pressure force, for both the high fidelity (HFM) and interpolation ROM solutions at $Re = 140$. Figure 9(b) shows the comparison of time-averaged pressure coefficient profile on the surface of cylinder at $Re = 140$. The Drag, Lift and pressure coefficients are estimated (respectively) as,

$$C_d = 2\int_{L_p} p_l \hat{x} dl; \quad C_l = 2\int_{L_p} p_l \hat{y} dl \quad \text{and} \quad C_p = 2(p - p_\infty) \tag{45}$$

Where L_p is the perimeter of cylinder, p_l is the pressure on the small segment

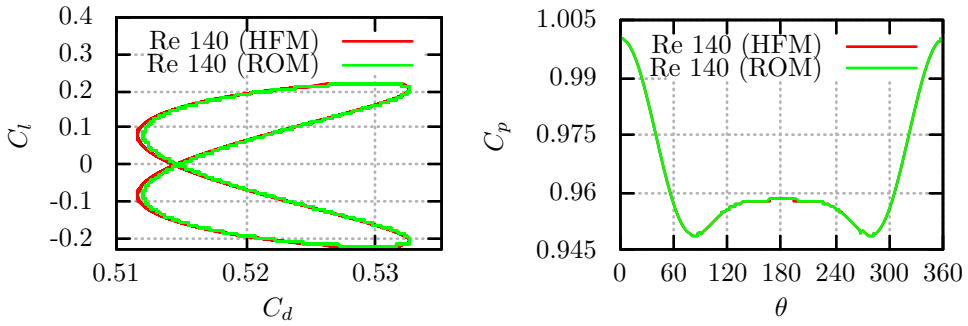

(a) Drag versus Lift coeff. comparison (b) Time-averaged pressure profile

Figure 9: Phase plot of drag Vs lift coeff. and surface pressure profile comparison

(dl) of the perimeter. $\hat{x}$, $\hat{y}$ are the projections of the unit vector normal to a length segment dl along the inflow (x) and flow normal (y) directions respectively.

The time signal of streamwise velocity in Figure 10(a) is probed at $x = 5, y = 0$. The time evolution of the Drag and Lift coefficients for unit cylinder length (estimated using pressure force only) is compared in Figure 10(b). It shows a fairly good agreement with the high fidelity CFD simulation results. The ROM time signals are $\sim 27\ T_{Re}$ long and they persist for any time duration (T_∞).

4. Summary

A simple and robust approach to the model reduction of Navier-Stokes equations is presented. In contrast to the Galerkin Reduced-Order Models (ROMs), the method is based on the periodicity of the Proper Orthogonal Decomposition (POD) time coefficients - a beautiful feature of the POD temporal basis functions (chronos) - in statistically stationary flows. In order to cope with the changing operating condition (such as Reynolds number) the reduced POD basis is interpolated using linear interpolation of the reference operating conditions. The error and stability analysis suggests that the errors in snapshot POD, truncation of higher POD modes and the linear interpolation are bounded for the time evolution. The total absolute error mainly depends on the difference in

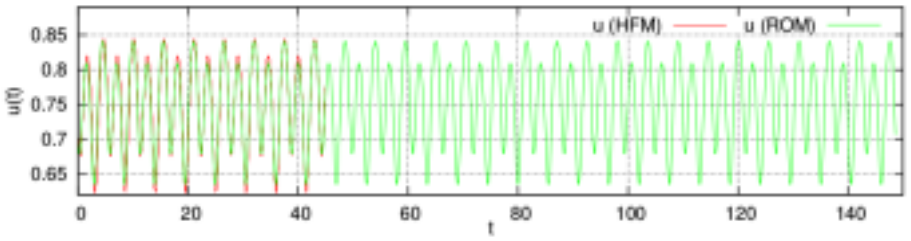

(a) Streamwise velocity at $x = 5, y = 0$

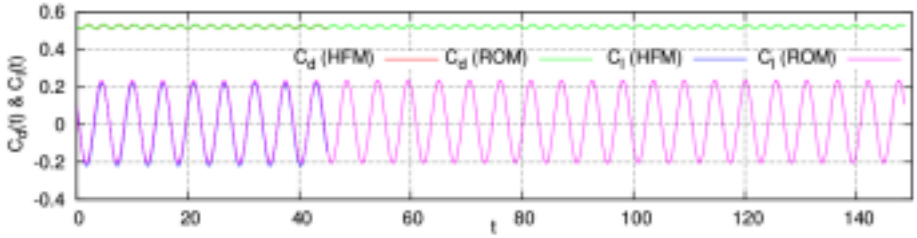

(b) Drag and Lift (pressure) force coeff.

Figure 10: Comparison of time signals of u, C_d and C_l

two reference states ($\Delta\eta$) and sensitivity of the flow to the operating parameter. The results of high fidelity CFD simulation of the flow past a cylinder show good agreements with the proposed method. The stable limit-cycles of the errors and the linear interpolation of reduced basis for changing operating condition ensure the stability and robustness of the interpolation ROM. Although we did consider a case study of 2-dimensional (2-D) incompressible flow, the mathematical formulation is developed for the full 3-D compressible Navier-Stokes equations. Further, each state variable is treated independently, therefore we anticipate the applicability of the method for wide range of problems with coupled phenomena (e.g. flow around aerofoil at high Mach, fluid-structure interaction).

Acknowledgement

The authors acknowledge Centre National de la Recherche Scientifique (CNRS) for facilitating the work via Agence Nationale de la Recherche (ANR) project Baresafe.

References

Aubry, N., 1991. On the hidden beauty of the proper orthogonal decomposition. Theoretical and Computational Fluid Dynamics 2, 339–352.

Aubry, N., Holmes, P., Lumley, J.L., Stone, E., 1988. The dynamics of coherent structures in the wall region of a turbulent boundary layer. Journal of Fluid Mechanics 192, 115–173.

Balajewicz, M., Dowell, E., 2012. Stabilization of projection-based reduced order models of the navierstokes. Nonlinear Dynamics 70, 1619–1632.

Bergmann, M., Bruneau, C.H., Iollo, A., 2009. Enablers for robust pod models. Journal of Computational Physics 228, 516–538.

Demmel, J., 1997. Applied Numerical Linear Algebra. Society for Industrial and Applied Mathematics.

Dumon, A., Allery, C., Ammar, A., 2013. Proper generalized decomposition method for incompressible navierstokes equations with a spectral discretization. Applied Mathematics and Computation 219, 8145 – 8162.

Holmes, P., Berkooz, G., Lumley, J.L., 1990. Turbulence, dynamical systems and the unreasonable effectiveness of empirical eigenfunctions, in: Proceedings of the International Congress of Mathematicians, Kyoto, pp. 1607–1617.

Joseph, D.D., 1976. Stability of fluid motions. i, ii. NASA STI/Recon Technical Report A 77, 12423.

Kunisch, K., Volkwein, S., 2002. Galerkin proper orthogonal decomposition methods for a general equation in fluid dynamics. SIAM Journal on Numerical analysis 40, 492–515.

Lassila, T.M., Manzoni, A., Quarteroni, A., Rozza, G., 2013. Model order reduction in fluid dynamics: challenges and perspectives, in: Quarteroni, A., Rozza, G. (Eds.), Reduced Order Methods for modeling and computational

reduction. Springer, Milano. MS&A, pp. 235–273. EPFL MATHICSE report 22.2013.

Lumley, J.L., 1967. The Structure of Inhomogeneous Turbulent Flows, in: Yaglom, A.M., Tatarski, V.I. (Eds.), Atmospheric turbulence and radio propagation. Nauka, Moscow, pp. 166–178.

Ma, X., Karniadakis, G.E., 2002. A low-dimensional model for simulating three-dimensional cylinder flow. Journal of Fluid Mechanics 458, 181–190.

Morzynski, M., Stankiewicz, W., Noack, B.R., Thiele, F., King, R., Tadmor, G., 2006. Generalized mean-field model for flow control using a continuous mode interpolation, in: Proceedings of the Third AIAA Flow Control Conference.

Noack, B.R., Afanasiev, K., Morzynski, M., Tadmor, G., Thiele, F., 2003. A hierarchy of low-dimensional models for the transient and post-transient cylinder wake. Journal of Fluid Mechanics 497, 335–363.

Noack, B.R., Eckelmann, H., 1994. A low-dimensional galerkin method for the three-dimensional flow around a circular cylinder. Physics of Fluids (1994-present) 6, 124–143.

Noack, B.R., Morzynski, M., Tadmor, G., 2011. Reduced-order modelling for flow control. volume 528. Springer.

Noack, B.R., Papas, P., Monkewitz, P.A., 2005. The need for a pressure-term representation in empirical galerkin models of incompressible shear flows. Journal of Fluid Mechanics 523, 339–365.

Rempfer, D., 2000. On low-dimensional galerkin models for fluid flow. Theoretical and Computational Fluid Dynamics 14, 75–88.

Rowley, C.W., Colonius, T., Murray, R.M., 2004. Model reduction for compressible flows using pod and galerkin projection. Physica D: Nonlinear Phenomena 189, 115–129.

Rowley, C.W., MEZIĆ, I., Bagheri, S., Schlatter, P., Henningson, D.S., 2009. Spectral analysis of nonlinear flows. Journal of Fluid Mechanics 641, 115–127.

Schmid, P.J., 2010. Dynamic mode decomposition of numerical and experimental data. Journal of Fluid Mechanics 656, 5–28.

Sirisup, S., Karniadakis, G., 2004. A spectral viscosity method for correcting the long-term behavior of pod models. Journal of Computational Physics 194, 92–116.

Sirisup, S., Karniadakis, G., 2005. Stability and accuracy of periodic flow solutions obtained by a pod-penalty method. Physica D: Nonlinear Phenomena 202, 218–237.

Sirovich, L., 1987. Turbulence and the dynamics of coherent structures. part i: Coherent structures. Quaterly of Applied Mathematics XLV, 561–571.

Turkel, E., Vatsa, V.N., Radespiel, R., 1996. Preconditioning methods for low-speed flows. National Aeronautics and Space Administration NASA CR 201605.